Chapter 9
Dynamical Cluster Approximation

H. Fotso, S. Yang, K. Chen, S. Pathak, J. Moreno, M. Jarrell, K. Mikelsons, E. Khatami, and D. Galanakis

Abstract The dynamical cluster approximation (DCA) is a method which systematically incorporates nonlocal corrections to the dynamical mean-field approximation. Here we present a pedagogical discussion of the DCA by describing it as a Φ-derivable coarse-graining approximation in k-space, which maps an infinite lattice problem onto a periodic finite-sized cluster embedded in a self-consistently determined effective medium. We demonstrate the method by applying it to the two-dimensional Hubbard model. From this application, we show evidences of the presence of a quantum critical point (QCP) at a finite doping underneath the superconducting dome. The QCP is associated with the second-order terminus of a line of first order phase separation transitions. This critical point is driven to zero temperature by varying the band parameters, generating the QCP. The effect of the proximity of the QCP to the superconducting dome is also discussed.

9.1 Introduction

Some of the most exotic properties of materials, including high-temperature super-conductivity, colossal magnetoresistance, and heavy Fermion and non-Fermi liquid

H. Fotso (✉) · S. Yang · K. Chen · S. Pathak · J. Moreno · M. Jarrell
Department of Physics and Astronomy, Louisiana State University, Baton Rouge,
LA 70803, USA
e-mail: herbert.fotso@gmail.com; yangphysics@gmail.com; kchen5@lsu.edu;
pathaksandeep@gmail.com; moreno@lsu.edu; jarrellphysics@gmail.com

K. Mikelsons · E. Khatami
Department of Physics, Georgetown University, Washington, DC 20057, USA
e-mail: karlis@physics.georgetown.edu; ehsankhatami@gmail.com

D. Galanakis
Division of Physics and Applied Physics, Nanyang Technological University of Singapore,
21 Nanyang Link, Singapore 637371
e-mail: dimitris.galanakis@gmail.com

behaviors, are due to strong electronic correlations. The materials which display these properties are characterized by either narrow electronic bands or compact orbitals with large angular momentum in the valence shell. In either case, the potential energy associated with some of these electronic degrees of freedom is comparable to or larger than their electronic kinetic energy (bandwidth), which invalidates conventional perturbative approaches. Thus, we resort to mean-field approximations, which we solve numerically so that diagrams to all orders are included, and we use them to study simplified models representing these systems.

For example, the Hubbard model [1–3] is the simplest model of a correlated electronic lattice system. Together with the $t - J$ model, they are thought to at least qualitatively describe some of the properties of transition metal oxides, and high-temperature superconductors [4]. The periodic Anderson model along with various Kondo lattice models has been proposed to describe both the actinide and lanthanide heavy fermion systems and the Kondo insulators. The Holstein model incorporates the essential physics of strongly interacting electrons and phonons. All of these model Hamiltonians contain at least two major ingredients: a local interaction term and a nonlocal hopping term. For example, the Hubbard model Hamiltonian (see Fig. 9.1) is

$$
\begin{aligned}
H = - t \sum_{\langle j,k \rangle \sigma} (c_{j\sigma}^\dagger c_{k\sigma} + c_{k\sigma}^\dagger c_{j\sigma}) + \epsilon \sum_j (n_{j\uparrow} + n_{j\downarrow}) \\
+ U \sum_j (n_{j\uparrow} - 1/2)(n_{j\downarrow} - 1/2) ,
\end{aligned}
\tag{9.1}
$$

where $c_{j\sigma}^\dagger$ ($c_{j\sigma}$) creates (destroys) an electron at a site j with a spin σ, $n_{i\sigma} = c_{i\sigma}^\dagger c_{i\sigma}$, t is the nearest neighbor hopping which sets the unit of energy and U is the on-site Coulomb repulsion between the electrons.

However, except for special limits, even such a simplified model like (9.1) cannot be solved exactly. For example, for the Hubbard model, no exact solutions exist except in one dimension, where the knowledge is in fact rather complete [5–7]. The periodic Anderson model is only solvable in the limit where the orbital degeneracy diverges [8], and the Holstein model is only solvable in the Eliashberg–Migdal limit where vertex corrections may be neglected. Clearly a new approach to these models is needed if nontrivial exact solutions are desired.

Metzner and Vollhardt [9, 10], Kuramoto [11, 12], and Müeller-Hartmann [13] suggested such a new approach based on a mean-field theory which becomes exact when the dimensionality $d = \infty$. The resulting formalism neglects dynamical

Fig. 9.1 Cartoon of the Hubbard model, characterized by a single band with near-neighbor hopping t, and local repulsion U

Fig. 9.2 Quantum cluster approaches, like the DMFA and DCA, map the infinite lattice problem onto a self-consistently embedded cluster problem
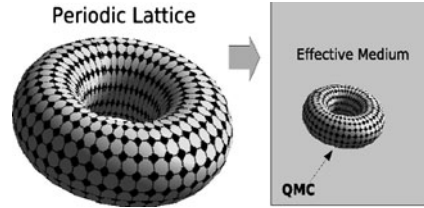
intersite correlations while retaining the important local dynamical correlations. The resulting formalism is called the dynamical mean field approximation (DMFA) since it may be employed in any dimension, but is only exact on infinite-dimensional lattices. In finite dimensions, the dynamical cluster approximation (DCA) is used to systematically study nonlocal corrections to the DMFA [14, 15]. Quantum cluster approaches, such as the DMFA and DCA, work by mapping an infinite periodic lattice onto a self-consistently embedded cluster problem, as illustrated in Fig. 9.2. Correlations up to the cluster size are treated explicitly, while those at longer length scales are treated in a mean-field level. The DMFA/DCA cluster problem may be solved by a variety of methods; however, quantum Monte Carlo (QMC) has been the first numerically exact solver employed [16] and remains the most powerful and adaptable method.

In this article, we will present a pedagogical discussion of the DCA and its relationship to the DMFA. In Sect. 9.2 we will first derive the DMFA as a coarse-graining approximation, extend this logic to derive the DCA and also provide a derivation from the Φ functional. In Sect. 9.3, we describe how physical quantities are calculated in this formalism. In Sect. 9.4 we will discuss applications of the DCA showing how it is used to find evidence for a quantum critical point (QCP) underneath the superconducting dome and to investigate the nature of this QCP and finally to study the relationship between superconductivity and the QCP.

9.2   The Dynamical Mean Field and Cluster Approximations

9.2.1   The Dynamical Mean-Field Approximation

The DCA algorithm can be derived in analogy with the DMFA. The DMFA is a local approximation which was used by Kuramoto in perturbative calculations as a simplification of the k-summations which render the problem intractable [11, 12]. But it was after the work of Metzner and Vollhardt [9] and Müller-Hartmann [13], who showed that this approximation becomes exact in the limit of infinite dimensions, that it received extensive attention. In this approximation, one neglects the spatial dependence of the self-energy, retaining only its variation with time. See the reviews by Pruschke et al. [17] and Georges et al. [18] for a more extensive treatment.

In this section, we will show that it is possible to re-interpret the DMFA as a coarse-graining approximation. The DMFA consists of mapping the original lattice problem to a self-consistent impurity problem. This is equivalent to averaging the Green functions used to calculate the irreducible diagrammatic insertions over the Brillouin zone. An important consequence of this averaging is that the self-energy and the irreducible vertices of the lattice are independent of the momentum. Hence, they are those of the impurity.

Müller-Hartmann [13] showed that this coarse-graining becomes exact in the limit of infinite dimensions. For Hubbard-like models, the properties of the bare vertex are completely characterized by the Laue function Δ which expresses the momentum conservation at each vertex. In a conventional diagrammatic approach

$$\Delta(\mathbf{k}_1, \mathbf{k}_2, \mathbf{k}_3, \mathbf{k}_4) = \sum_{\mathbf{r}} \exp\left[i\mathbf{r} \cdot (\mathbf{k}_1 + \mathbf{k}_2 - \mathbf{k}_3 - \mathbf{k}_4)\right]$$

$$= N\delta_{\mathbf{k}_1+\mathbf{k}_2, \mathbf{k}_3+\mathbf{k}_4}, \tag{9.2}$$

where $\mathbf{k}_1$ and $\mathbf{k}_2$ ($\mathbf{k}_3$ and $\mathbf{k}_4$) are the momenta entering (leaving) each vertex through its Green function legs. However, as the dimensionality $D \to \infty$ Müller-Hartmann showed that the Laue function reduces to [13]

$$\Delta_{D \to \infty}(\mathbf{k}_1, \mathbf{k}_2, \mathbf{k}_3, \mathbf{k}_4) = 1 + \mathcal{O}(1/D). \tag{9.3}$$

The DMFA assumes the same Laue function, $\Delta_{\text{DMFA}}(\mathbf{k}_1, \mathbf{k}_2, \mathbf{k}_3, \mathbf{k}_4) = 1$, even in the context of finite dimensions. Thus, the conservation of momentum at internal vertices is neglected and we may freely sum over the internal momentum labels of each Green function leg. This leads to a collapse of the momentum dependent contributions and only local terms remain.

This argument may then be applied to the generating functional Φ, which is the sum over all closed connected compact graphs constructed from the dressed Green's function G and the bare interaction. The second-order contribution to Φ for a Hubbard-like model is illustrated in Fig. 9.3. The self-energy Σ may be obtained from a functional derivative of Φ with respect to the Green's function G, which effectively removes one of the Green's function lines (Fig. 9.4).

The perturbative series for Φ, Σ and the irreducible vertices Γ in the DMFA are identical to those of the corresponding impurity model, so that conventional
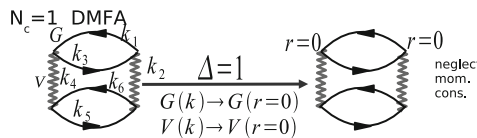

Fig. 9.3 The second-order contribution to the generating functional Φ. As we apply the DMFA coarse-graining approximation, (9.3), Φ becomes a functional of the local Green's function and interaction

Fig. 9.4 The DMFA self-energy contains only local corrections. See, e.g., the third graph. To prevent overcounting these contributions, the local self-energy must be excluded, cf. (9.4), from the Green's function line used in most cluster solvers
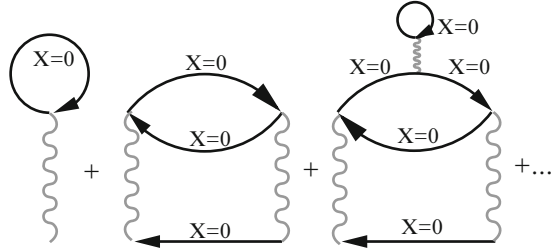
impurity solvers may be used. However, since most impurity solvers can be viewed as methods that sum all the graphs, not just the skeletal ones, it is necessary to exclude Σ from the local propagator input, $\mathcal{G}$, to the impurity solver, in order to avoid overcounting local self-energy contributions. Therefore, in Matsubara frequencies

$$\mathcal{G}(i\omega_n)^{-1} = G(i\omega_n)^{-1} + \Sigma(i\omega_n), \qquad (9.4)$$

where $i\omega_n = (2n + 1)\pi T$, $\Sigma(i\omega_n)$ is the self-energy and $G(i\omega_n)$ the full local Green's function. Hence, in the local approximation, the Hubbard model has the same diagrammatic expansion as an Anderson impurity with a bare local propagator $\mathcal{G}(i\omega_n; \Sigma)$, which is determined self-consistently.

An algorithm constructed from this approximation is the following: (1) An initial guess for $\Sigma(i\omega_n)$ is chosen (usually from the perturbation theory). (2) $\Sigma(i\omega_n)$ is used to calculate the corresponding local Green's function

$$G(i\omega_n) = \int d\eta \frac{\rho^0(\eta)}{i\omega_n - (\eta - \mu) - \Sigma(i\omega_n)}, \qquad (9.5)$$

where ρ^0 is the noninteracting density of states, and μ is the chemical potential. (3) Starting from $G(i\omega_n)$ and $\Sigma(i\omega_n)$ used in the second step, the host Green's function $\mathcal{G}(i\omega_n)^{-1} = G(i\omega_n)^{-1} + \Sigma(i\omega_n)$ is calculated, which serves as the bare Green's function of the impurity model. (4) Starting with $\mathcal{G}(i\omega_n)$, the local Green's function $G(i\omega_n)$ is obtained using the QMC method (or another technique). (5) Using the QMC output for the cluster Green's function $G(i\omega_n)$ and the host Green's function $\mathcal{G}(i\omega_n)$ from the third step, a new $\Sigma(i\omega_n) = \mathcal{G}(i\omega_n)^{-1} - G(i\omega_n)^{-1}$ is calculated, which is then used in step (2) to reinitialize the process. Steps (2)–(5) are repeated until convergence is reached. If in step (4) the QMC algorithm of Hirsch and Fye [19, 20] is used to compute the local Green's function $G(\tau)$ or other physical quantities in imaginary time, local dynamical quantities are then calculated by analytically continuing the corresponding imaginary-time quantities using the maximum-entropy method (MEM) [21].

9.2.2 *The Dynamical Cluster Approximation*

Like the DMFA, the DCA may be intuitively motivated with a coarse-graining transformation. In the DMFA, the propagators used to calculate Φ and its derivatives were coarse-grained over the entire Brillouin zone, leading to local (momentum independent) irreducible quantities. In the DCA, we wish to relax this condition, and systematically restore momentum conservation and nonlocal corrections. Thus, in the DCA, the reciprocal space of the lattice which contains N points is divided into N_c cells of identical linear size Δk. The coarse-graining transformation is set by averaging the Green function within each cell. If $N_c = 1$ the original lattice problem is mapped to an impurity problem (DMFA). If N_c is larger than one, then nonlocal corrections of length $\approx \pi/\Delta k$ to the DMFA are introduced. Provided that the propagators are sufficiently weakly momentum dependent, this is a good approximation. If N_c is chosen to be small, the cluster problem can be solved using conventional techniques such as the QMC, the non-crossing approximation (NCA) or the fluctuation exchange approximation (FLEX). This averaging process also establishes a relationship between the systems of size N and N_c. A simple choice, which will be discussed in Sect. 9.2.3, is to equate the irreducible quantities (self-energy, irreducible vertices) of the cluster to those in the lattice.

This coarse-graining procedure and the relationship of the DCA to the DMFA is illustrated by a microscopic diagrammatic derivation of the DCA. The DCA systematically restores the momentum conservation at internal vertices relinquished by the DMFA. The Brillouin zone is divided into $N_c = L^D$ cells of linear size $\Delta k = 2\pi/L$ (cf. Fig. 9.5 for $N_c = 8$). Each cell is represented by a cluster momentum $\mathbf{K}$ in the center of the cell. We require that momentum conservation be (partially) observed for momentum transfers between cells, i.e., for momentum transfers larger than Δk, but neglected for momentum transfers within a cell, i.e., less than Δk. This requirement can be established by using the Laue function [15]

$$\Delta_{\text{DCA}}(\mathbf{k}_1, \mathbf{k}_2, \mathbf{k}_3, \mathbf{k}_4) = N_c \delta_{\mathbf{M}(\mathbf{k}_1)+\mathbf{M}(\mathbf{k}_2),\mathbf{M}(\mathbf{k}_3)+\mathbf{M}(\mathbf{k}_4)}, \tag{9.6}$$

Fig. 9.5 Coarse-graining cells for $N_c = 8$ (differentiated by alternating fill patterns) that partition the first Brillouin zone (*dashed line*). Each cell is centered on a cluster momentum $\mathbf{K}$ (*filled circles*). To construct the DCA cluster, we map a generic momentum in the zone such as $\mathbf{k}$ to the nearest cluster point $\mathbf{K} = \mathbf{M}(\mathbf{k})$ so that $\tilde{\mathbf{k}} = \mathbf{k} - \mathbf{K}$ remains in the cell around $\mathbf{K}$
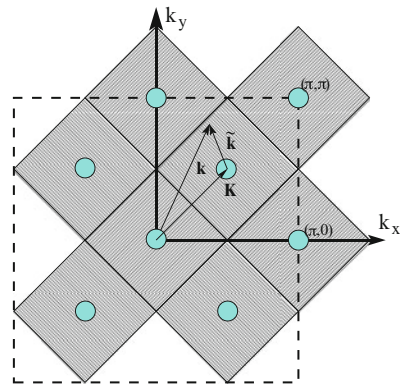
where $\mathbf{M}(\mathbf{k})$ is a function which maps $\mathbf{k}$ onto the momentum label $\mathbf{K}$ of the cell containing $\mathbf{k}$ (see Fig. 9.5). This choice for the Laue function systematically interpolates between the exact result, (9.2), which it recovers when $N_c \to N$ and the DMFA result, (9.3), which it recovers when $N_c = 1$. With this choice of the Laue function the momenta of each internal leg may be freely summed over the cell.

This is illustrated for the second-order term in the generating functional in Fig. 9.6. Each internal leg $G(\mathbf{k})$ in a diagram is replaced by the coarse-grained Green function $\bar{G}(\mathbf{M}(\mathbf{k}))$, defined by

$$\bar{G}(\mathbf{K}) \equiv \frac{N_c}{N} \sum_{\tilde{\mathbf{k}}} G(\mathbf{K} + \tilde{\mathbf{k}}), \qquad (9.7)$$

where N is the number of points of the lattice, N_c is the number of cluster $\mathbf{K}$ points, and the $\tilde{\mathbf{k}}$ summation runs over the momenta of the cell about the cluster momentum $\mathbf{K}$ (see Fig. 9.5). The diagrammatic consequences for the generating functional and its derivatives are unchanged; however, the complexity of the problem is greatly reduced since $N_c \ll N$.

9.2.3 Φ Derivability

The coarse-graining approximation can be applied to the generating functional Φ. The generating functional is the sum over all of the closed connected compact diagrams, such as the one shown in Fig. 9.6. It is defined as

$$\Phi(G) = \sum_{l,\sigma} p_l \, tr\left[\Sigma_\sigma^l G_\sigma\right]. \qquad (9.8)$$

The trace indicates summation over frequency, momentum and spin. Here, Σ_σ^l is the set of irreducible self-energy diagrams of lth order in the interaction, G_σ is the dressed Green function related to Σ_σ by the Dyson equation $G_\sigma^{-1} = G_\sigma^{0-1} - \Sigma_\sigma$,
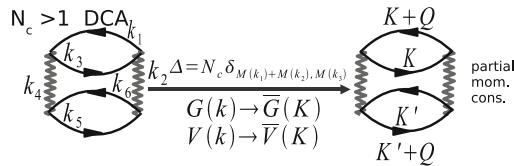

Fig. 9.6 A second-order term in the generating functional of the Hubbard model. Here the *undulating line* represents the interaction U, and on the LHS (RHS) the *solid line* the lattice (coarse-grained) single-particle Green functions. When the DCA Laue function is used to describe momentum conservation at the internal vertices, the momenta collapse onto the cluster momenta and each lattice Green function is replaced by the coarse-grained result

where G^0 is the noninteracting Green function, p_l is a counting factor equal to the number of occurrences of G_σ in each term (for Hubbard-like models, $p_l = 1/l$). The free energy F can be expressed as

$$F = -k_B T \left(\Phi(G) - \text{tr}[\Sigma_\sigma G_\sigma] - \text{tr} \ln[-G_\sigma] \right). \tag{9.9}$$

With the above definition, it holds that $\Sigma_\sigma = \delta\Phi/\delta G_\sigma$, as required for a "$\Phi$-derivable" theory, and the free energy is stationary under variations of G. In addition, the irreducible vertex function is obtained by a second variation of Φ, $\Gamma_{\sigma\sigma'} = \delta^2\Phi/\delta G_\sigma \delta G_{\sigma'} = \delta\Sigma_\sigma/\delta G_{\sigma'}$.

The DCA can be microscopically motivated by the choice of the Laue function Δ_{DCA} (1.6). Within this formalism, the effect of the chosen Laue function is the replacement of the self-energy Σ_σ and the irreducible vertex $\Gamma_{\sigma,\sigma'}$ by the corresponding coarse-grained quantities (indicated here by the bars). Consider for example the Schwinger–Dyson equation relating the self-energy to the two-particle reducible vertex $T^{(2)}$, $\Sigma = GGGT^{(2)}$. The vertices connecting the Green function to $T^{(2)}$ do not preserve momentum conservation within the cells about the cluster momentum due to the DCA Laue function. Consequently, the lattice Green function G_σ is replaced by the coarse-grained Green function $\bar{G}_\sigma$. The external momentum label (**k**) of the self-energy is in principle still a lattice momentum; however, the self-energy will only depend on **k** through the function **M(k)**. If we use this self-energy in the calculation of its contribution to the Φ functional, the Laue function on the vertices will "reduce" both the self-energy as well as the closing Green function to their corresponding coarse-grained expressions. Consequently, the DCA Φ functional reads

$$\Phi_{\text{DCA}}(G) = \sum_l p_l tr\left[\bar{\Sigma}^l_\sigma \bar{G}_\sigma\right]. \tag{9.10}$$

In correspondence to the lattice system,

$$\frac{\delta\Phi_{\text{DCA}}}{\delta\bar{G}_\sigma} = \bar{\Sigma}_\sigma = \frac{\delta\Phi_{\text{DCA}}}{\delta G_\sigma}, \tag{9.11}$$

where the second equality follows since the variation $\delta/\delta G_\sigma$ corresponds to cutting a Green function line , so that $\delta\bar{G}_{\sigma\mathbf{K}}/\delta G'_\sigma\mathbf{k}' = \delta_{\mathbf{K},\mathbf{M(k')}}\delta_{\sigma,\sigma'}$. It follows that the DCA estimate of the free energy is

$$F_{\text{DCA}} = -k_B T \left(\Phi_{\text{DCA}} - \text{tr}[\Sigma_\sigma G_\sigma] - \text{tr} \ln[-G_\sigma] \right), \tag{9.12}$$

F_{DCA} is stationary with respect to $\mathbf{G}_\sigma$ when

$$\frac{-1}{k_B T}\frac{\delta F_{\text{DCA}}}{\delta G_\sigma(\mathbf{k})} = \bar{\Sigma}_\sigma(\mathbf{M(k)}) - \Sigma_\sigma(\mathbf{k}) = 0, \tag{9.13}$$

which means that $\Sigma(\mathbf{k}) = \bar{\Sigma}_\sigma(\mathbf{M}(\mathbf{k}))$ is the proper approximation for the lattice self-energy corresponding to Φ_{DCA}. The corresponding lattice single-particle propagator is then given by

$$G(\mathbf{k}, z) = \frac{1}{z - (\epsilon_\mathbf{k} - \mu) - \bar{\Sigma}(\mathbf{M}(\mathbf{k}), z)}, \tag{9.14}$$

where $\epsilon_\mathbf{k}$ is the quasiparticle energy, and μ the chemical potential. A similar procedure is used to construct the two-particle quantities needed to determine the phase diagram or the nature of the dominant fluctuations that can eventually destroy the high-temperature ground state. This procedure is a generalization of the method of calculating response functions in the DMFA [16, 22].

The introduction of the momentum dependence in the DCA self-energy allows one to detect some precursors to transitions which are absent in the DMFA; but for the actual determination of the nature of the instability, one needs to compute the response functions. These susceptibilities are thermodynamically defined as second derivatives of the free energy with respect to external fields. $\Phi_{\mathrm{DCA}}(G)$ and $\bar{\Sigma}_\sigma$, and hence F_{DCA} depend on these fields only through G_σ and the bare G_σ^0. Following Baym and Kadanoff [23], it is easy to verify that, the approximation

$$\Gamma_{\sigma,\sigma'} \approx \bar{\Gamma}_{\sigma,\sigma'} \equiv \delta\bar{\Sigma}_\sigma / \delta G_{\sigma'} \tag{9.15}$$

yields the same estimate that would be obtained from the second derivative of F_{DCA} with respect to the applied field. For example, the first derivative of the free energy with respect to a spatially homogeneous external magnetic field h is the magnetization,

$$m = \mathrm{Tr}\left[\sigma G_\sigma\right]. \tag{9.16}$$

The susceptibility is given by the second derivative,

$$\chi = \frac{\partial m}{\partial h} = \mathrm{Tr}\left[\sigma \frac{\partial G_\sigma}{\partial h}\right]. \tag{9.17}$$

We substitute $G_\sigma = \left(G_\sigma^{0-1} - \bar{\Sigma}_\sigma\right)^{-1}$, and evaluate the derivative,

$$\chi = \mathrm{Tr}\left[\sigma \frac{\partial G_\sigma}{\partial h}\right] = \mathrm{Tr}\left[G_\sigma^2\left(1 + \sigma \frac{\partial\bar{\Sigma}_\sigma}{\partial G_{\sigma'}}\frac{\partial G_{\sigma'}}{\partial h}\right)\right]. \tag{9.18}$$

We can generalize this argument to include the staggered susceptibility by identifying $\chi_{\sigma,\sigma'} = \sigma \frac{\partial G_{\sigma'}}{\partial h}$, and $\chi_{\mathrm{st}} = Tr[\chi_{\sigma,-\sigma}]$ and $\chi_\sigma^0 = G_\sigma^2$. By collecting all the terms within both traces, and sum over the cell momenta $\tilde{\mathbf{k}}$, we obtain the two-particle Dyson's equation

$$2\left(\bar{\chi}_{\sigma,\sigma} - \bar{\chi}_{\sigma,-\sigma}\right)$$
$$= 2\bar{\chi}_\sigma^0 + 2\bar{\chi}_\sigma^0\left(\bar{\Gamma}_{\sigma,\sigma} - \bar{\Gamma}_{\sigma,-\sigma}\right)\left(\bar{\chi}_{\sigma,\sigma} - \bar{\chi}_{\sigma,-\sigma}\right). \tag{9.19}$$

We see that again it is the irreducible quantity, i.e., the vertex function, for which the cluster and lattice quantities are equal.

9.2.4 Algorithm

A variety of techniques may be used to sum the cluster diagrams in order to calculate the cluster self-energy, Σ_c, and the cluster vertex function, Γ_c. In the past, we have used the QMC [24], the non-crossing approximation [25] or the Fluctuation-Exchange approximation [26]. Here, we will mainly use QMC techniques. Since QMC is systematically exact; i.e., it effectively sums all diagrams to all orders, care must be taken when defining the initial Green function (the solid lines in Fig. 9.6) to avoid overcounting diagrams on the cluster. For example, to fourth order and higher in perturbation theory for the self-energy, nontrivial self-energy corrections enter in the diagrammatic expansion for the cluster self energy of the Hubbard model. To avoid overcounting these contributions, we must first subtract off the self-energy corrections on the cluster from the Green function line used to calculate Σ_c and its functional derivatives. This cluster-excluded Green function is given by

$$\frac{1}{\mathcal{G}(\mathbf{K}, z)} = \frac{1}{\bar{G}(\mathbf{K}, z)} + \Sigma_c(\mathbf{K}, z) \tag{9.20}$$

which is the coarse-grained Green function with correlations on the cluster excluded. Since $\Sigma_c(\mathbf{K}, z)$ is not known a priori, it must be determined self-consistently, starting from an initial guess, usually from the perturbation theory. This guess is used to calculate $\bar{G}$ from (9.7). $\mathcal{G}(\mathbf{K}, z)$ is then calculated with (9.20), and it is used to initialize the QMC calculation. The QMC estimate for the cluster self energy is then used to calculate a new estimate for $\bar{G}(\mathbf{K})$ using (9.7). The corresponding $\mathcal{G}(\mathbf{K})$ is used to reinitialize the procedure which continues until $G_c = \bar{G}$ and the self-energy converges to the desired accuracy.

One of the difficulties encountered in earlier attempts to include nonlocal corrections to the DMFA was that these methods were not causal [27, 28]. The spectral weight was not conserved and the imaginary parts of the one-particle retarded Green functions and self-energies were not negative definite as required by causality. The DCA algorithm presented in this subsection does not present these problems. This algorithm is fully causal as shown by Hettler et al. [15]. They analyze the different steps of the self-consistent loop and found that none of them breaks the causality of the Green functions. Starting from the QMC block, one can see that if the input $\mathcal{G}$ is causal, since the QMC algorithm is essentially exact, the output G_c will also be causal. Then the corresponding $\Sigma_c(\mathbf{K}, i\omega_n)$ is causal. This in turn ensures that the coarse-grained Green function $\bar{G}(\mathbf{K}, i\omega_n)$ also fulfills causality. The only nontrivial operation which may break causality is the calculation of $\mathcal{G}(\mathbf{K}, i\omega_n)$. Hettler et al. [15] used a geometric proof to show that even this part of the loop respects causality.

9.3 Physical Quantities

Most experiments measure quantities which can be expressed as reducible one or two-particle Green's functions. As discussed above, the appropriate way to calculate these quantities is to first extract the corresponding irreducible quantity from the cluster calculation, and then use it to calculate the reducible quantity. For example, to calculate the single-particle Green's function (relevant for angle-resolved photoemission spectroscopy) we first extract the cluster self-energy and use the Dyson equation to construct the lattice Green's function. To calculate the phase diagram, we calculate the irreducible vertices in the different scattering channels Γ, and insert them into the Bethe–Salpeter equations for the lattice. In this subsection we will provide more details about the relationship between the lattice and cluster two-particle Green's functions and describe how a lattice susceptibility may be calculated efficiently.

9.3.1 Particle–Hole Channel

As a specific example, we will describe the calculation of the two-particle particle–hole Green's function

$$
\chi_{\sigma,\sigma'}(q,k,k') = \int_0^\beta \int_0^\beta \int_0^\beta \int_0^\beta d\tau_1 d\tau_2 d\tau_3 d\tau_4
$$
$$
\times e^{i\left((\omega_n+\nu_n)\tau_1 - \omega_n\tau_2 + \omega_{n'}\tau_3 - (\omega_{n'}+\nu_n)\tau_4\right)}
$$
$$
\times \langle T_\tau c^\dagger_{\mathbf{k}+\mathbf{q}\sigma}(\tau_1) c_{\mathbf{k}\sigma}(\tau_2) c^\dagger_{\mathbf{k}'\sigma'}(\tau_3) c_{\mathbf{k}'+\mathbf{q}\sigma'}(\tau_4)\rangle,
$$

where we adopt the conventional notation [29] $k = (\mathbf{k}, i\omega_n)$, $k' = (\mathbf{k}, \omega_n')$, $q = (\mathbf{q}, \nu_n)$ and T_τ is the time ordering operator.

$\chi_{\sigma,\sigma'}(q,k,k')$ and $\Gamma_{\sigma,\sigma'}(q,k,k')$ are related to each other through the Bethe–Salpeter equation (Fig. 9.7):

$$
\chi_{\sigma,\sigma'}(q,k,k') = \chi^0_{\sigma,\sigma'}(q,k,k') + \chi^0_{\sigma,\sigma''}(q,k,k'')
$$
$$
\times \Gamma_{\sigma'',\sigma'''}(q,k'',k''') \chi_{\sigma''',\sigma'}(q,k''',k'), \qquad (9.21)
$$

where frequency labels have been suppressed, and $\Gamma_{\sigma,\sigma'}(q,k,k')$ is the two-particle irreducible vertex which is the analogue of the self-energy, $\chi^0_{\sigma,\sigma'}(q,k,k'')$ is the noninteracting susceptibility constructed from a pair of fully dressed single-particle Green's functions. As usual, a summation is to be made for repeated indices.

We now make the DCA substitution $\Gamma_{\sigma,\sigma'}(q,k,k') \to \Gamma_{c\sigma,\sigma'}(q,\mathbf{M}(k),\mathbf{M}(k'))$ in (9.21). We ultimately want to sum over all k and k' to calculate the susceptibility at q. Note that after the DCA substitution only the bare and dressed two-particle
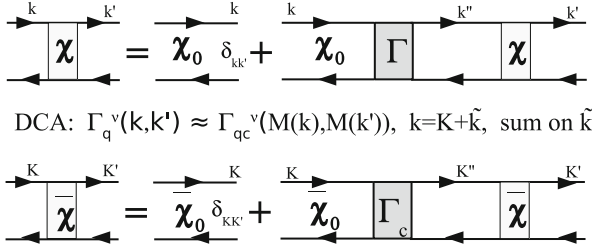
Fig. 9.7 The Bethe–Salpeter equation in the DCA. We approximate the lattice irreducible vertex Γ^ν by the Γ_c^ν from the DCA cluster and coarse-grain over the momentum $\tilde{\mathbf{k}}$. The remaining equation is a function only of the cluster momenta $\mathbf{K}$ and may be solved by inversion

Green's functions χ depend upon the momenta $\tilde{\mathbf{k}}$ within a cell. Since χ and χ^0 in the product on the RHS of (9.21) share no common momentum labels, we may now freely sum over the momenta $\tilde{\mathbf{k}}$ within a cell, yielding

$$\bar{\chi}_{\sigma,\sigma'}(q, K, K') = \bar{\chi}^0_{\sigma,\sigma'}(q, K, K') + \bar{\chi}^0_{\sigma,\sigma''}(q, K, K'')$$
$$\times \Gamma_{c\sigma'',\sigma'''}(q, K'', K''')\bar{\chi}_{\sigma''',\sigma'}(q, K''', K'). \quad (9.22)$$

By coarse-graining the Bethe–Salpeter equation, we have greatly reduced its complexity; each of the matrices above is sufficiently small that they may be easily manipulated using standard techniques.

In contrast with the single-particle case where the coarse-grained quantities are identical to those of the cluster, $\chi_{c\sigma,\sigma'}(q, K, K')$ is not equal to $\bar{\chi}_{\sigma,\sigma'}(q, K, K')$. This is because the self-consistency is made only at the single-particle level. Unlike the single-particle case where both $\Sigma(K)$ and $\bar{G}(K)$ are directly calculated, only the cluster susceptibility is calculated by the cluster solver, neither $\Gamma_{\sigma,\sigma'}(q, K, K')$ nor the coarse-grained susceptibility $\bar{\chi}_{\sigma,\sigma'}(q, K, K')$ is calculated during the self-consistency. Instead, the coarse-grained noninteracting susceptibility $\bar{\chi}^0_{\sigma,\sigma'}(q, K, K')$ is calculated in a separate program after the DCA converges using the following relation

$$\bar{\chi}^0_{\sigma,\sigma'}[(\mathbf{q}, i\nu_n); (\mathbf{K}, i\omega_n); (\mathbf{K}', i\omega'_n)] = \delta_{\sigma,\sigma'}\delta_{\mathbf{K},\mathbf{K}'}\delta_{\omega_n,\omega'_n} \frac{N_c}{N} \sum_{\tilde{\mathbf{k}}} G_\sigma(\mathbf{K} + \tilde{\mathbf{k}}, i\omega_n)$$
$$\times G_\sigma(\mathbf{K} + \tilde{\mathbf{k}} + \mathbf{q}, i\omega_n + \nu_n). \quad (9.23)$$

The vertex function is extracted by inverting the cluster two-particle Bethe–Salpeter equation

$$\chi_{c\sigma,\sigma'}(q, K, K') = \chi^0_{c\sigma,\sigma'}(q, K, K') + \chi^0_{c\sigma,\sigma''}(q, K, K'')$$
$$\times \Gamma_{c\sigma'',\sigma'''}(q, K'', K''')\chi_{c\sigma''',\sigma'}(q, K''', K'). \quad (9.24)$$

If we combine (9.24) and (9.22), then the coarse-grained susceptibility may be obtained after the elimination of $\Gamma(\mathbf{q}, \mathbf{K}, \mathbf{K}')$ between the two equations. It reads

$$\bar{\chi}^{-1} = \chi_c^{-1} - \chi_c^{0^{-1}} + \bar{\chi}^{0^{-1}},$$

where, for example, $\bar{\chi}$ is the matrix formed from $\bar{\chi}_{\sigma,\sigma'}(\mathbf{q}, \mathbf{K}, \mathbf{K}')$ for fixed $\mathbf{q}$. The charge (ch) and spin (sp) susceptibilities $\chi_{ch,sp}(\mathbf{q}, T)$ are deduced from $\bar{\chi}$

$$\chi_{ch,sp}(q, T) = \frac{(k_B T)^2}{N_c^2} \sum_{KK'\sigma\sigma'} \lambda_{\sigma\sigma'} \bar{\chi}_{\sigma,\sigma'}(q, K, K'), \qquad (9.25)$$

where $\lambda_{\sigma\sigma'} = 1$ for the charge channel and $\lambda_{\sigma\sigma'} = \sigma\sigma'$ for the spin channel.

9.3.2 Particle–Particle Channel

The calculation of susceptibilities in the particle–particle channel is essentially identical to the above equation. The exception to this rule occurs when we calculate susceptibilities for transitions to states of lower symmetry than the lattice symmetry. For example, in order to obtain the pairing susceptibility of the desired symmetry (s, p, d), the two-particle Green's function must be multiplied by the corresponding form factors $g(\mathbf{k})$ and $g(\mathbf{k}')$. In the study of the Hubbard model below, we will be particularly interested in $g(\mathbf{k}) = 1$ (s wave), $g(\mathbf{k}) = \cos(k_x) + \cos(k_y)$ (extended s wave) and $g(\mathbf{k}) = \cos(k_x) - \cos(k_y)$ ($d_{x^2-y^2}$ wave). These symmetries have been evoked as possible candidates for the superconducting ground state of cuprate superconductors (Fig. 9.8).

These factors modify the Bethe–Salpeter equations

$$g(\mathbf{k})\chi(q, k, k')g(\mathbf{k}') = g(\mathbf{k})\chi^0(q, k, k')g(\mathbf{k}') + g(\mathbf{k})\chi^0(q, k, k'')$$
$$\times \Gamma(q, k'', k''') \times \chi(q, k''', k')g(\mathbf{k}'), \qquad (9.26)$$

where

$$\chi(q, k, k') = \int_0^\beta \int_0^\beta \int_0^\beta \int_0^\beta d\tau_1 d\tau_2 d\tau_3 d\tau_4$$
$$\times e^{i\left((\omega_n+\nu_n)\tau_1 - \omega_n\tau_2 + \omega_{n'}\tau_3 - (\omega_{n'}+\nu_n)\tau_4\right)}$$
$$\times \langle T_\tau c^\dagger_{\mathbf{k}+\mathbf{q}\sigma}(\tau_1)c^\dagger_{-\mathbf{k}-\sigma}(\tau_2)c_{-\mathbf{k}'-\sigma}(\tau_3)c_{\mathbf{k}'+\mathbf{q}\sigma}(\tau_4)\rangle. \qquad (9.27)$$

On the LHS, we have dropped the spin indices since we will consider only opposite-spin pairing. Equation (9.26) cannot be easily solved if it is coarse-grained, since this will partially convolve $\chi(q, k, k')$ with *two* factors of g on the LHS and
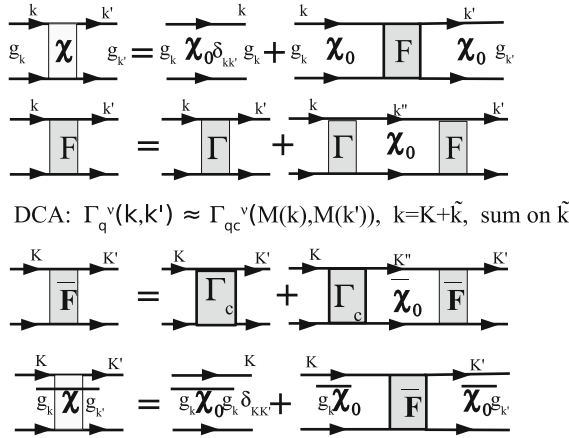
Fig. 9.8 Calculation of particle–particle projected susceptibilities. Often we want to calculate a projected particle–particle susceptibility (e.g., d-wave, with $g_{\mathbf{k}} = \cos(k_x) - \cos(k_y)$). Here the Bethe–Salpeter equation is rewritten in terms of the reducible vertex F. We approximate the lattice irreducible vertex Γ^ν by the Γ_c^ν from the DCA cluster and coarse-grain over the $\tilde{k}$. Then the projected bare bubbles are calculated, and the remaining equation is a function of the cluster $\mathbf{K}$ only and may be solved by inversion

one factor on the RHS. Hence for the pairing susceptibilities, or for any situation where nontrivial form factors must be used, we use the equivalent equation involving the reducible vertex F (instead of the irreducible vertex Γ)

$$
\begin{aligned}
g(\mathbf{k})\chi(q,k,k')g(\mathbf{k}') &= g(\mathbf{k})\chi^0(q,k,k')g(\mathbf{k}') \\
&\quad + g(\mathbf{k})\chi^0(q,k,k'') \\
&\quad \times F(q,k'',k''')\chi^0(q,k''',k')g(\mathbf{k}'),
\end{aligned}
\tag{9.28}
$$

where

$$
\begin{aligned}
F(q,k,k') &= \Gamma(q,k,k') \\
&\quad + \Gamma(q,k,k'')\chi^0(q,k'',k''')\Gamma(q,k''',k') + \cdots
\end{aligned}
\tag{9.29}
$$

We define

$$
\Pi_{g,g}(q,k,k') = g(\mathbf{k})\chi(q,k,k')g(\mathbf{k}')
\tag{9.30}
$$

$$
\Pi_{g,g}^0(q,k,k') = g(\mathbf{k})\chi^0(q,k,k')g(\mathbf{k}')
\tag{9.31}
$$

$$
\Pi_g^0(q,k,k') = g(\mathbf{k})\chi^0(q,k,k').
\tag{9.32}
$$

The remaining steps of the calculation are similar to the particle–hole case. We invert the cluster particle–particle Bethe–Salpeter equation with $g = 1$ for the

cluster, in order to extract Γ_c. We then coarse-grain (9.29) and use Γ_c to calculate the coarse-grained $\bar{F} = \Gamma_c \left(1 - \bar{\chi}^0 \Gamma_c\right)^{-1}$. We then coarse-grain (9.28), and use the coarse-grained $\bar{F}$ to calculate the coarse-grained $\bar{\Pi}_{g,g}$

$$\bar{\Pi}_{g,g}(q, K, K') = \bar{\Pi}_{g,g}^0(q, K, K')$$
$$+ \bar{\Pi}_g^0(q, K, K'')\bar{F}(q, K'', K''')\bar{\Pi}_g^0(q, K''', K'). \quad (9.33)$$

The pairing susceptibility of a desired symmetry is given by

$$P_g(q, T) = \frac{(k_B T)^2}{N_c^2} \sum_{K, K'} \bar{\Pi}_{gg}(q, K, K'). \quad (9.34)$$

9.4 DCA and Quantum Criticality in the Hubbard Model

9.4.1 Evidence of the Quantum Critical Point at Optimal Doping

The phase diagram of the hole-doped cuprates exhibits some unusual properties including a pseudogap (PG) at low doping and unusual metallic behavior at higher doping. This has lead researchers to postulate the existence of a QCP at optimal doping in the cuprates phase diagram. Some investigators have also argued that the PG is related with the establishment of order [30–35], and the optimal doping is in the proximity of the QCP associated to this order. Others have argued that the QCP is located at the transition from the non-Fermi liquid (NFL) to the Fermi liquid (FL) ground state with no order established in the PG region [36]. We use the DCA to explore the presence of this QCP in the two-dimensional Hubbard model [37]. Investigating the single-particle properties, we find further evidence for the QCP and determine that it is the terminus of a V-shaped marginal Fermi liquid (MFL) region separating the NFL PG region from the FL region at high doping.

In this section we analyze several physical quantities using the known forms of the self-energy in the MFL and the FL regions, as well as an ansatz in the region beyond but near the QCP, when the system crosses over from MFL to FL. Within the DCA we can evaluate $Z_0(\mathbf{k}) = (1 - \text{Im}\Sigma(\mathbf{k}, i\omega_0)/\omega_0)^{-1}$, where $\omega_0 = \pi T$ is the lowest Fermion Matsubara frequency. For a well behaved self-energy, $\lim_{T \to 0} Z_0(\mathbf{k}) = Z(\mathbf{k})$ is the quasiparticle renormalization factor. In this problem, the relevant low energy scales are the antiferromagnetic exchange energy J near half-filling, the PG temperature T^* in the PG region, and the effective Fermi energy T_X at higher doping. From the previously described analysis [38], we find that $J_{\text{eff}} \approx 0.44t$ for $n = 0.95$ and $n = 1$. We extract T^* and T_X from fits to the data[37], as presented in the figures below, where data for $T \ll J_{\text{eff}}$ are included in each case. T^* can be also determined from the peak in the susceptibility (see Fig. 9.9).
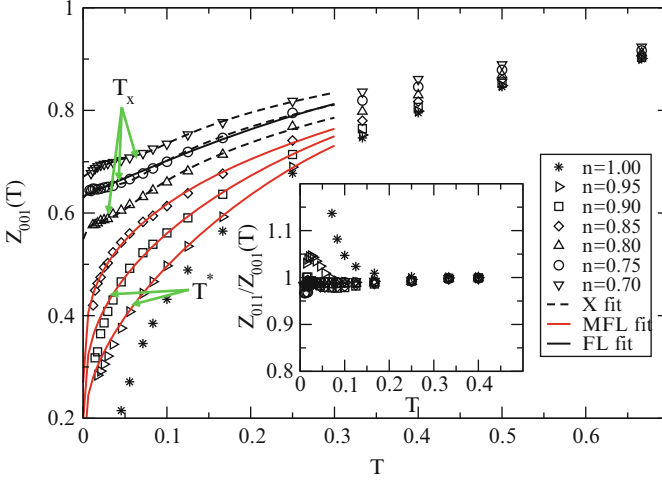
Fig. 9.9 (Taken from [37]) The single-particle density of states in the pseudogap region for various temperatures with $n = 0.95$, $U = 6t = 1.5$, $W = 8t = 2$. The unit of energy is set to $4t = 1$. Inset: The bulk, $\mathbf{Q} = 0$, cluster susceptibility for the same parameters. The PG in the DOS begins to develop at roughly the same temperature T^* which identifies the peak susceptibility

The quasiparticle fraction is calculated with $\mathbf{k}$ on the Fermi surface (FS) as defined by the maximum along the $(1, 1)$ and $(0, 1)$ directions of $|\nabla n(\mathbf{k})|$. This FS is slightly different from the one identified using the spectral function $A(\mathbf{k}, \omega = 0)$ [39] when $n > 0.85$. However, the quasiparticle weights $Z \rightarrow 0$ everywhere on both Fermi surfaces (and shows a similar anisotropy on both). So, our conclusions do not depend on whether $|\nabla n(\mathbf{k})|$ or $A(\mathbf{k}, \omega = 0)$ is used to identify the FS. Since we are interested in the crossover from PG to FL behavior, and the PG is stronger along the $(0, 1)$ direction, we present detailed results and analysis for the $(0, 1)$ direction only. The quasiparticle fraction along the $(0, 1)$ direction, Z_{001}, is shown in the main panel in Fig. 9.10 for different fillings.

As the filling n increases through $n = 0.85$, the low-temperature Matsubara quasiparticle data changes its behavior. The data have a negative curvature at all T for $n > 0.85$; while for $n < 0.85$, the data have a negative curvature at high T and develops a weak positive curvature at lower T. The change in curvature of the low temperature data for $n < 0.85$ is easily understood as a crossover to an FL region. On the other hand, the MFL always has a negative curvature. So at the transition between FL and MFL, a region of positive curvature is found at $T \approx T_X$. The ratio of the quasiparticle fraction at the FS along the (01) and the (11) direction, Z_{011}/Z_{001}, plotted in the inset of Fig. 9.10 as a function of temperature for different fillings shows that the conclusions from the above analysis are not specific to the direction $(0, 1)$. The ratio is seen to be essentially the same for all fillings at the QCP, indicating that Z is essentially isotropic at the QCP, and becomes progressively more anisotropic as we dope into the PG region. Furthermore, Z calculated at $\mathbf{k} = (0, \pi)$
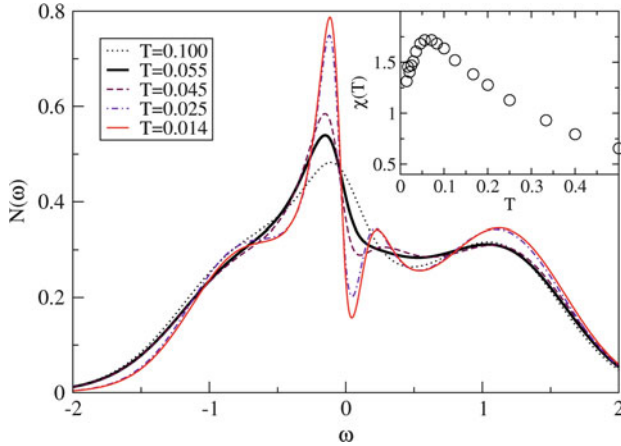
Fig. 9.10 (Taken from [37]) Matsubara quasiparticle fraction $Z_0(\mathbf{k})$ versus temperature T evaluated with $\mathbf{k}$ on the Fermi surface along the $(0, 1)$ direction for different fillings n when $U = 6t$ and the bandwidth $W = 8t$. The unit of energy is such that $4t = 1$. The *lines* represent fits in the region $T < 0.3$ to either the MFL form, for $n \geq 0.85$, or the crossover form (X), for $n < 0.85$. The *arrows* indicate the values T_X extracted from the crossover fit or T^* (cf. Figs. 9.9 and 9.11). Note that the data for $n = 0.85$ fit the MFL nearly perfectly, while the data for $n > 0.85$ are poorly fit by the MFL for $T < T^*$ because, due to the formation of the pseudogap, the MFL temperature dependence is too slow to provide a good fit. The data for $n = 0.75$ were also fit by the FL form; however, the fit is clearly worse than that obtained by the crossover form. *Inset*: The ratio, Z_{011}/Z_{001}, is plotted as a function of temperature for different fillings. The ratio is essentially the same for all fillings at the QCP, indicating that Z is essentially isotropic, and becomes progressively more anisotropic as we dope into the PG region

(not shown) is qualitatively the same as that calculated along the 01 direction on the FS. Therefore, the QCP, which separates the low-temperature FL phase from the PS region, cannot be an artifact of the interpolation nor due to the change of the Fermi wavevector with filling. Rather, it is due to a dramatic change in the nature of the self-energy for momenta near the FS.

The PG region, $n > 0.85$, is further characterized by exploring the temperature dependence of the density of states (DOS) and the bulk, $\mathbf{Q} = 0$, spin susceptibility of the cluster, as shown in Fig. 9.9 and its inset, respectively. A concomitant depression appears in the low energy DOS at temperatures below the energy, T^*, of the peak in the susceptibility. The corresponding $Z_{001}(T)$ is well fit with the MFL form for $T > T^*$, while it fits poorly for $T < T^*$ (Fig. 9.10) due to the formation of the PG.

In Fig. 9.11, we show the relevant temperatures near the QCP, T_X and T^*. T_X is determined from the fits while T^* is determined from the peak in the susceptibility and the initial appearance of the PG in the DOS as shown in Fig. 9.9. Here, T_c is the superconducting critical temperature determined in [40] from the divergence of the pairing susceptibilities as discussed in Sect. 9.3.2.

Further evidence of the presence of the QCP separating the FL region from the NFL PG region can be obtained by studying the thermodynamics of the system [41].
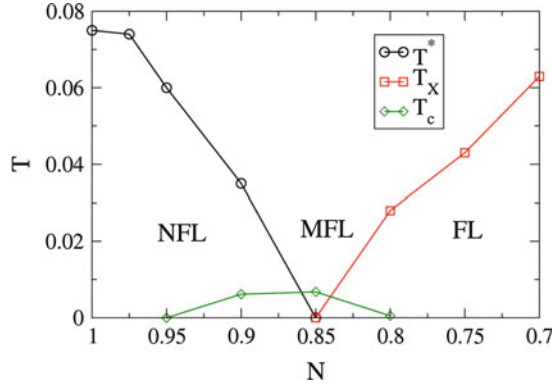
Fig. 9.11 (Taken from [37]) The pseudogap temperature T^*, identified from the peak in the susceptibility and the emergence of the PG in the DOS shown in Fig. 9.9. The FL to MFL crossover temperature identified by fits to the Matsubara quasiparticle data shown in Fig. 9.10. T_c is the superconducting critical temperature determined in [40] from the divergence of the pairing susceptibilities as discussed in Sect. 9.3.2. The unit of energy is set to $4t = 1$

The Hubbard model can be rewritten as:

$$H = \sum_{\mathbf{k}\sigma} \epsilon_{\mathbf{k}}^0 c_{\mathbf{k}\sigma}^\dagger c_{\mathbf{k}\sigma} + U \sum_i n_{i\uparrow} n_{i\downarrow}, \tag{9.35}$$

where $\epsilon_{\mathbf{k}}^0 = -2t \left(\cos k_x + \cos k_y \right)$ is the tight binding dispersion. The quadratic part of the Hamiltonian, referred to as the kinetic energy, and the potential energy may be calculated as [42]

$$E_k = \frac{T}{N} \sum_{\omega_n, \mathbf{k}, \sigma} \epsilon_{\mathbf{k}}^0 G_\sigma(\mathbf{k}, i\omega_n) \tag{9.36}$$

$$E_p = \frac{T}{2N} \sum_{\omega_n, \mathbf{k}, \sigma} \Sigma_\sigma(\mathbf{k}, i\omega_n) G_\sigma(\mathbf{k}, i\omega_n), \tag{9.37}$$

Both E_k and E_p are expected to exhibit a leading T^2 low temperature behavior in the FL region and $T^2 \ln T$ behavior [43] in the MFL region. continuous time quantum Monte Carlo (CTQMC) is used to solve the cluster problem and the energies are calculated using (9.36) and (9.37). CTQMC avoids systematic errors and prevents them from accumulating between different temperatures in the calculation of the entropy given by partial integration:

$$S(\beta, n) = S(0, n) + \beta E(\beta, n) - \int_0^\beta E(\beta', n) \mathrm{d}\beta', \tag{9.38}$$

where $S(0, n) = -n \ln \frac{n}{2} - (2 - n) \ln \left(1 - \frac{n}{2}\right)$, n is the filling, $\beta = 1/T$ and E is the total energy obtained by summing up E_{p} and E_{k} [44]. Since DCA preserves thermodynamical consistency [45], our entropy results also satisfy the Maxwell relation

$$\left(\frac{\partial S}{\partial n}\right)_{T,U} = -\left(\frac{\partial \mu}{\partial T}\right)_{U,n}, \tag{9.39}$$

where μ is the chemical potential.

The behavior of the numerically calculated potential energy (E_{p}) and kinetic energy (E_{k}) is consistent with the analytical expressions in the FL and MFL regions. However, we find that the characteristic energy scales of the FL and PG vanish at the QC doping where the MFL behavior persists to the lowest accessible temperature. This is consistent with the existence of a QCP at zero temperature between the FL and PG regions. To illustrate this we fit the total energy away from half-filling to the form:

$$E(T) = E(0) + A f(T) T^2 + B \left(1 - f(T)\right) T^2 \ln \frac{T}{\Omega}, \tag{9.40}$$

where $f(T) = 1/\left(\exp\left((T - T_X)/\theta\right) + 1\right)$ describes the crossover from the MFL to the quadratic behavior, characteristic of an FL or presumably a PG region. A, B, θ, T_X and Ω are the fitting parameters of the QMC energy data, as shown in Fig. 9.12. The fit is indistinguishable from the data for all fillings at low T. In agreement with the previous estimates, these fits indicate that $T_{\mathrm{FL}} \approx 0.15t$ for $n = 0.70$ and $T^* \approx 0.24t$ for $n = 0.95$.
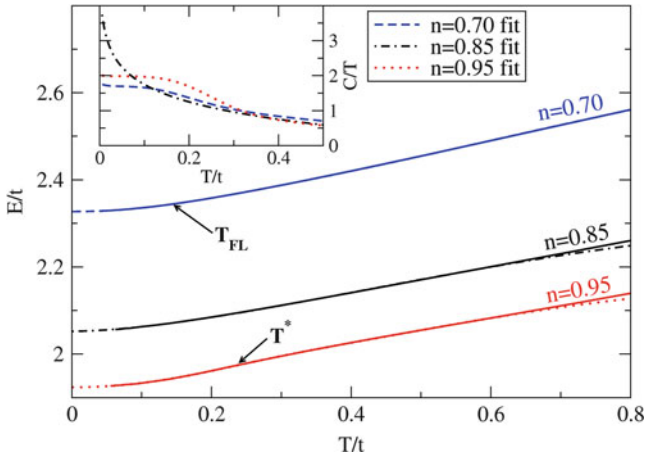

Fig. 9.12 (Taken from [41]) Total energy per site, E, versus temperature for different fillings. The data are fit to a crossover form of the energy, (9.40) (*dashed lines*). The values of T_X determined from the fit are indicated as T_{FL} for $n = 0.70$ and T^* for $n = 0.95$. In the inset, the specific heat calculated from the fit is plotted versus temperature
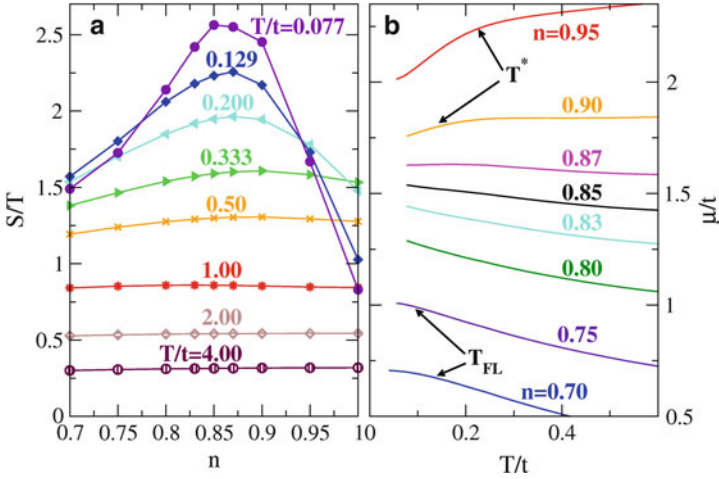
Fig. 9.13 (Taken from [41]) *Left panel*: filling dependence of S/T showing emergence of a peak at $n = 0.85$ at low temperatures. *Right panel*: Chemical potential versus temperature for a range of fillings with PG and FL energy scales shown as T^* and T_{FL} for $n = 0.95$ and $n = 0.70$, respectively. Note that the position of the maximum of entropy in the *left panel* corresponds to $\partial\mu/\partial T = 0$ in the *right panel*. As the temperature is lowered, the maximum of entropy shifts towards lower n, causing a local particle–hole symmetry for $n = 0.85$ at low T (see text)

The calculation of the specific heat is known to be a very difficult problem. It usually involves a fit of $E(T)$ to a regularized (smooth) functional form [46, 47]. In the present case, we already have an excellent fit, so C/T is simply obtained from a derivative of the fit divided by temperature. For $n = 0.70$, at low temperatures, C/T is flat in T, as one expects for an FL. The data in the PG region, $n = 0.95$, also show this behavior, but, at the critical filling, $n = 0.85$, the data show a weak divergence at low T consistent with quantum critical behavior [41].

The behavior of the entropy per site near the critical filling as the system is cooled confirms the physics seen in C/T with no need for a fit or a numerical derivative. With decreasing T, the entropy is more strongly quenched in the FL and PG regions than in the MFL region, creating a maximum in S/T at $n = 0.85$ and low temperature (see Fig. 9.13a). The persistent rise of S/T at critical doping as $T \rightarrow 0$ is consistent with the increase to C/T. The near overlap for $n < 0.85$ of the low temperature S/T at different temperatures also agrees with the constant C/T indicative of a FL.

Equation (9.39) indicates that a local maximum in S/T versus n corresponds to a flat chemical potential as a function of temperature. For this reason, the critical filling at low T can be identified from the temperature dependence of μ for different fillings. This is shown in Fig. 9.13b, where one can see that the near temperature independence of μ at $n = 0.90$ for $0.25t < T < 0.50t$ evolves into a broad maximum centered around $T = 0.15t$ for $n = 0.87$ which presumably moves to $n = 0.85$ at low enough temperatures. These observations are consistent with the

evolution of the maximum in S/T versus n as the temperature is lowered from $0.50t$ to $0.08t$ (see Fig. 9.13a). A stationary chemical potential can be the signature of a local particle–hole symmetry, in analogy with the half-filled case. This is consistent with the observation of near particle–hole symmetry in the cuprates in the proximity of optimal doping [36].

9.4.2 Nature of the Quantum Critical Point in the Hubbard Model

A systematic study of the phase diagram of the Hubbard model as a function of additional control parameters allows us to identify the nature of the QCP in the cuprates. We use an extended Hubbard model where the tight binding dispersion is modified to include t', the hopping between next-nearest neighbors. The dispersion is then $\epsilon_{\mathbf{k}}^0 = -2t\left(\cos k_x + \cos k_y\right) - 4t'\left(\cos k_x \cos k_y - 1\right)$. Our results suggest that the QCP is the zero-temperature limit of a line of second-order phase separation transition as shown schematically in Fig. 9.14 [48]. The control parameter for this transition is t'.

To illustrate this, we calculate the filling, n, versus μ and the compressibility (or bulk charge susceptibility), $dn/d\mu$, by taking its numerical derivative. To connect with previous results, simulations were performed with $U = 6t$ (Fig. 9.15a), but, as discussed previously [48], the region of divergent charge fluctuations is larger and more accessible for $U = 8$ and cluster size $N_c = 8$. For this reason, we also present results for these parameters where additional studies have been conducted
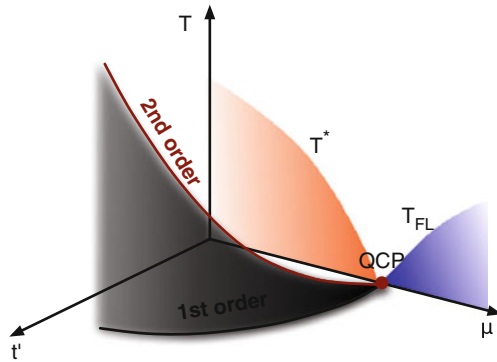

Fig. 9.14 (Taken from [48]) Schematic phase diagram of the 2D Hubbard model in the temperature (T), chemical potential (μ) and next-near-neighbor hopping (t') space. For $t' > 0$ the first-order phase separation transition terminates at a second-order critical point at doping n_c and temperature T_{ps}. The line of second-order critical points (T_{ps}, n_c) approaches the QCP on the $t' = 0$ plane. This is the critical point separating the pseudogap (PG) from the Fermi liquid (FL) region
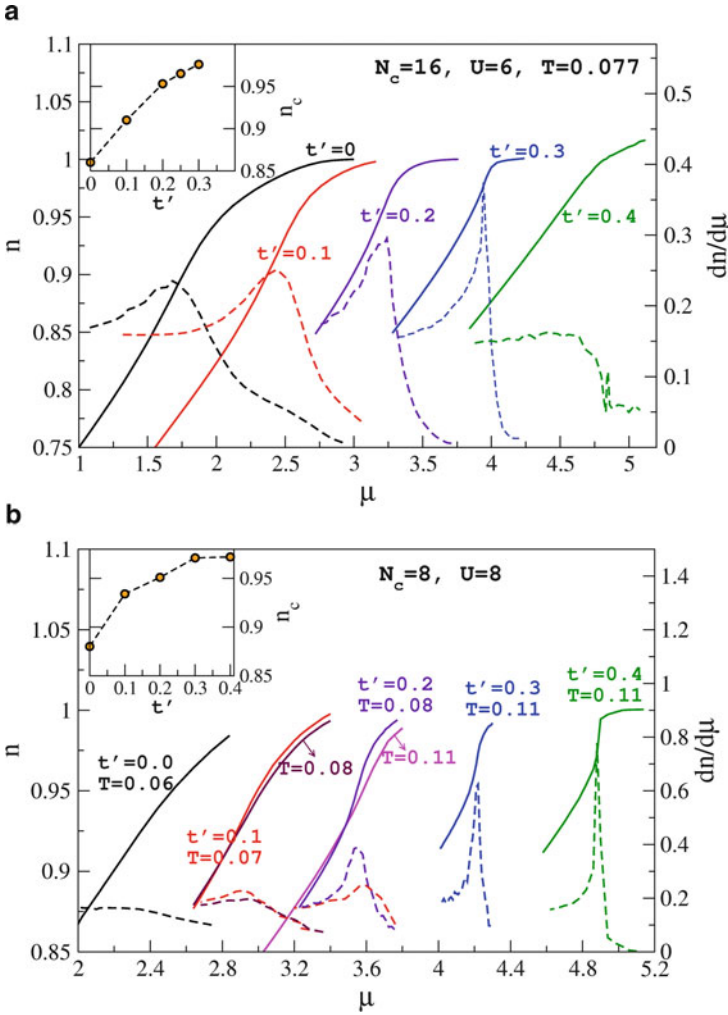
Fig. 9.15 (Taken from [48]) Filling, n (*solid lines*), and compressibility, $dn/d\mu$ (*dashed lines*), plotted versus chemical potential, μ, for various values of t' for (**a**) $U = 6$, $N_c = 16$ and $T = 0.077$ and (**b**) $U = 8$, $N_c = 8$ at different temperatures. The unit of energy is t. The critical filling, where the compressibility peaks, is plotted in the corresponding inset. In (**a**), when $t' \to 0$, the peak in the charge susceptibility is located at the QCP identified previously [37]

(cf. Fig. 9.15b). Figure 9.15a shows n versus μ for $U = 6t$, $T = 0.077t$ and t' ranging from 0.0 to 0.4. The filling n increases monotonically with μ and shows a pronounced flat region associated with the Mott gap, especially for $t' < 0.4$. An inflection appears in $n(\mu)$ at finite doping and becomes more pronounced as t' increases. It translates into a peak in the susceptibility that becomes sharper and moves closer to half-filling as t' is increased. The peak in the susceptibility and the

plateau in $n(\mu)$ near half-filling disappear for $t' > 0.3$. In the inset, we plot n_c, the value of the critical filling at the peak as a function of t'. For $t' = 0$, $n_c = 0.86$ is in agreement with the filling of the QCP ($n_c = 0.85$) found previously for these parameters [37,41]. These results suggest an association between the QCP and charge fluctuations.

For temperatures below a critical temperature T_c, the filling is observed to develop a hysteresis as a function of μ. As mentioned before, the DCA equations are solved self-consistently starting with an initial guess for the self-energy, usually zero, the result from a higher temperature or that of perturbation theory. The solution is generally unique and independent from the initial guess for doping away from a critical doping δ_c, such as 0 or 10% doping. However, we find that for a critical chemical potential μ_c, if the initial self-energy is that corresponding to the undoped solution ($n = 1$), then n versus μ will look as the upper curve (squares) in Fig. 9.16, whereas if it is that of a large doping solution ($n < 1$), n versus μ will be described by the lower curve (circles) in Fig. 9.16. The fully converged self-energy from a previous point is used to initialize the calculation in both cases.

To further investigate the association between the QCP and charge fluctuations, we study the behavior of the bulk charge susceptibility, $\chi_c(\mathbf{Q} = 0, T)$, and its divergence as $t' \to 0$. We follow the line of second order critical points of these first order transitions as t' changes using χ_c as shown in Fig. 9.17. We plot the inverse
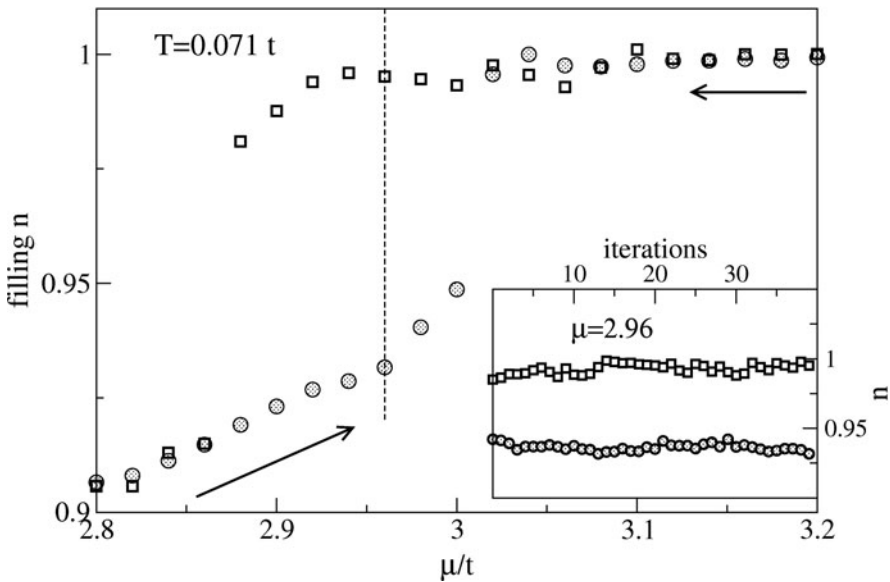

Fig. 9.16 (Taken from [49]) Filling n versus chemical potential for $t' = 0.3t$ at $T = 0.071\,t$ and $N_c = 8$. Two solutions describing a hysteresis are found, one incompressible with $n \approx 1$ (*squares*) and other a doped one (*circles*). *Inset*: stability of the two solutions versus DCA iterations when $\mu = 2.96t$ (middle of the hysteresis, corresponding to the *dotted line* in the main figure)
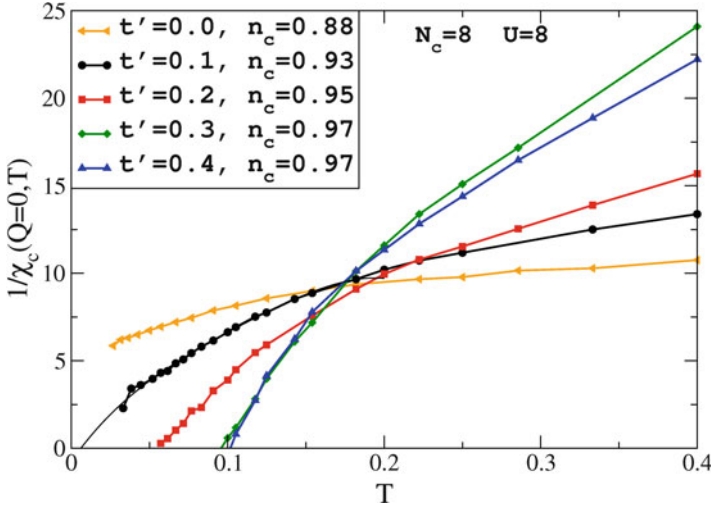
Fig. 9.17 (Taken from [48]) Inverse bulk charge susceptibility versus temperature when $U = 8t$, $N_c = 8$ for several values of t'. The unit of energy is t. The values of the critical filling n_c shown in the legend correspond to the maximum of the low temperature compressibility, or the filling where it first diverges

charge susceptibility at n_c as a function of temperature for different values of t' and $U = 8t$, $N_c = 8$. The critical filling n_c shown in the legend is the filling where the compressibility either diverges or is peaked at the lowest accessible temperature. The temperature of the second-order critical point is found to increase and move towards half-filling as t' is increased. However, in these results, unlike those of $U = 6t$ (Fig. 9.15a), the critical point seems to avoid half-filling even for $t' = 0.4t$. As can be seen in the persistence of the flat region in $n(\mu)$ near $n = 1$ for $t' = 0.4t$, the stronger Coulomb interaction $U = 8t$ also appears to strengthen the Mott gap for this value of t' (Fig. 9.15b).

The evidence discussed here strongly favors an interpretation involving a QCP as opposed to a simple crossover from the FL to an NFL as the filling increases towards one. The fits to the quasiparticle fraction $Z_0(\mathbf{k})$, the behavior of the DOS, the $T^2 ln T$ behavior of the kinetic and potential energies, the peak in S/T which sharpens as T falls, and the logarithmic behavior of the specific heat are clear signatures of quantum criticality. The results also show that the QCP is the terminal point of a line of second-order critical points associated with first-order phase separation transitions. The critical temperature is driven to zero as $t' \to 0$.

9.4.3 Relationship Between Superconductivity and the Quantum Critical Point

The critical doping at which the QCP is identified appears to be in close proximity to the optimal superconducting doping, as found in the Hubbard model [48] or in

the $t - J$ model [50]. Although this proximity might indicate that the QCP enhances pairing, the mechanism of such an enhancement remains unclear. Using DCA, we attempt to separate two different scenarios about the role of the QCP in the super-conducting mechanism [40]. The *first*, the quantum critical BCS (QCBCS) proposed by She and Zaanen [51], argues that the presence of the QCP leads to a replacement of the BCS logarithmic divergence of the pairing bubble by an algebraic divergence, resulting in a stronger pairing instability and a higher critical temperature compared to the BCS result for the same pairing interaction. The *second* scenario suggests that the pairing interaction is mediated by remnant fluctuations [52, 53]. This would be translated into a strongly enhanced pairing interaction in the vicinity of the QCP. We find that near the QCP, the pairing interaction depends monotonically on the doping and shows no special feature, whereas the pairing susceptibility acquires an algebraic dependence on the temperature. These findings are consistent with the first scenario.

The superconducting transition temperature T_c for a conventional BCS supercon-ductor is determined by the condition $V\chi'_0(\omega = 0) = 1$, where χ'_0 is the real part of the $q = 0$ bare pairing susceptibility and V is the strength of the pairing interaction. The transition is driven by the divergence of $\chi'_0(\omega = 0)$ which for a FL is given by $\chi'_0(T) \propto N(0) \ln(\omega_D / T)$, where $N(0)$ is the single-particle DOS at the Fermi surface and ω_D is the phonon Debye cutoff frequency. This leads to the well-known BCS superconducting transition formula, $T_c = \omega_D \exp[-1/(N(0)V)]$. We will use the same T_c equation $V\chi'_0(\omega = 0) = 1$ to analyze our results for the Hubbard model and look for the possibility that $\chi'_0(\omega = 0) \sim 1/T^\alpha$.

This analysis starts with the Bethe–Salpeter equation for the pairing channel:

$$\chi(Q)_{P,P'} = \chi_0(Q)_P \delta_{P,P'} + \sum_{P''} \chi(Q)_{P,P''} \Gamma(Q)_{P'',P'} \chi_0(Q)_{P'}, \quad (9.41)$$

where χ is the dynamical susceptibility, $\chi_0(Q)_P$ $[= -G(P + Q)G(-P)]$ is the bare susceptibility, which is constructed from G, the dressed one-particle Green's function, Γ is the vertex function, and indices $P^{[...]}$ and external index Q denote both momentum and frequency as discussed in Sect. 9.3.1. The divergence of the susceptibility is detected by solving the eigenvalue equation $\Gamma \chi_0 \phi = \lambda \phi$ [54] for fixed Q. By decreasing the temperature the leading eigenvalue λ increases reaching one at a temperature T_c, where the system undergoes a phase transition.

In order to be able to identify whether χ_0 or Γ dominates at the phase transition, we will make a BCS approximation and project them onto the d-wave pairing channel, which was found to be dominant [55, 56]. For χ_0, the d-wave projection is given by

$$\chi_{0d}(\omega) = \frac{\sum_k \chi_0(\omega, q = 0)_k g_d(k)^2}{\sum_k g_d(k)^2}, \quad (9.42)$$

where $g_d(k) = (\cos(k_x) - \cos(k_y))$ is the d-wave form factor. For the pairing strength we use the d-wave projection:

$$V_d = \frac{\sum_{k,k'} g_d(k)\Gamma_{k,k'}g_d(k')}{\sum_k g_d(k)^2} \tag{9.43}$$

using Γ at the lowest Matsubara frequency [57].

We further explore the different contributions to the strength of the pairing vertex V_d by performing an exact decomposition of Γ into its different cross-channels and projecting out the d-wave contribution of each contribution [57, 58]. The cross-channels include the fully irreducible vertex Λ, the charge channel ($S = 0$) contribution Φ_c and the spin channel ($S = 1$) contribution Φ_s. This follows from the fact that the vertex can be written as

$$\Gamma = \Lambda + \Phi_c + \Phi_s. \tag{9.44}$$

The d-wave projection as described above then gives

$$V_d = V_d^\Lambda + V_d^c + V_d^m. \tag{9.45}$$

We use $U = 6t$ ($4t = 1$) for both the $N_c = 12$ and $N_c = 16$ clusters. For these clusters, as found in the previous section, evidences of the QCP are observed around a doping of $\delta \approx 0.15$. In Fig. 9.18, we show the eigenvalues λ for different channels (magnetic, charge, and pairing) at the critical doping as a function of temperature. The results, for both cluster sizes, indicate a superconducting transition around $T_c = 0.007$ and an enhancement of the charge susceptibility with decreasing temperatures as can be expected from the QCP that arises as a terminus of a line of second-order phase separation transitions.

In Fig. 9.19, we present the strength of V_d as a function of doping for a range of temperatures. Here it is found that V_d decreases monotonically with increasing
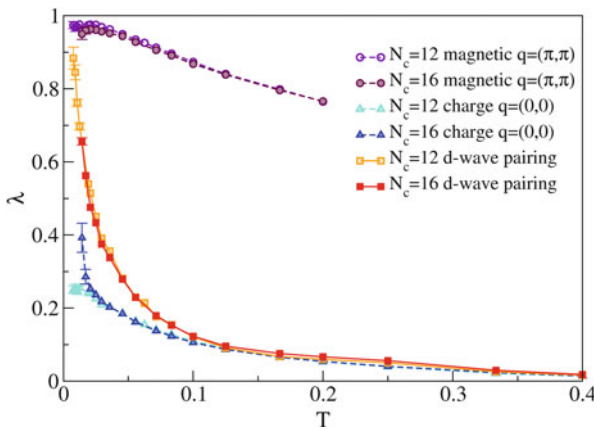

Fig. 9.18 (Taken from [40]) Plots of leading eigenvalues for different channels at the critical doping for $N_c = 12$ and $N_c = 16$ site clusters. The energy is set to $4t = 1$
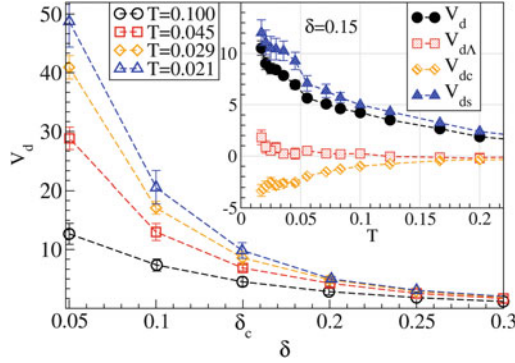
Fig. 9.19 (Taken from [40]) Plots of V_d, the strength of the d-wave pairing interaction, for various temperatures with $U = 6t$ and $N_c = 16$, where $4t = 1$. V_d decreases monotonically with doping, and shows no feature at the critical doping. In the inset are plots of the contributions to V_d from the charge V_d^c and spin V_d^s cross-channels and from the fully irreducible vertex V_d^Λ versus T at the critical doping. As the temperature is lowered, $T \ll J \approx 0.11 = 0.44t$, the contribution to the pairing interaction from the spin channel is clearly dominant
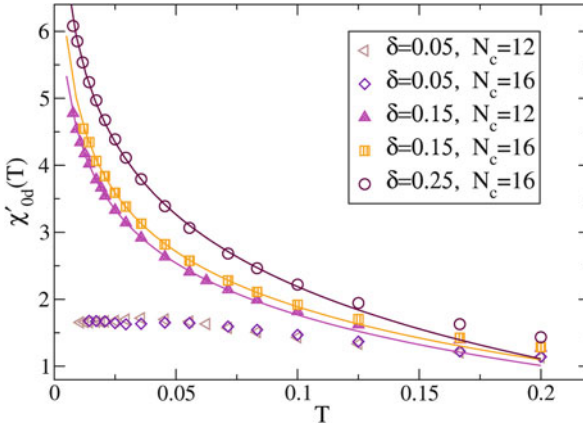

Fig. 9.20 (Taken from [40]) Plots of $\chi'_{0d}(\omega = 0)$, the real part of the bare d-wave pairing susceptibility at zero frequency, versus temperature at three characteristic values of the doping. The *solid lines* are fits to $\chi'_{0d}(\omega = 0) = B/\sqrt{T} + A \ln(\omega_c/T)$ for $T < J$. In the underdoped case ($\delta = 0.05$), $\chi'_{0d}(\omega = 0)$ does not grow with decreasing temperature. At the critical doping ($\delta = \delta_c = 0.15$), $\chi'_{0d}(\omega = 0)$ shows power-law behavior with $B = 0.04$ for the 12 site and $B = 0.09$ for the 16-site clusters (in both $A = 1.04$ and $\omega_c = 0.5$). In the overdoped region ($\delta = 0.25$), a log divergence is found, with $B = 0$ obtained from the fit

doping as seen in a previous study [59]. V_d does not show any feature at the critical doping $\delta_c = 0.15$. This effectively rules out the second scenario mentioned above. The different components in the inset suggest that V_d at the QCP originates predominantly from the spin channel. This behavior is similar to what was found previously while studying the pairing interaction [59].
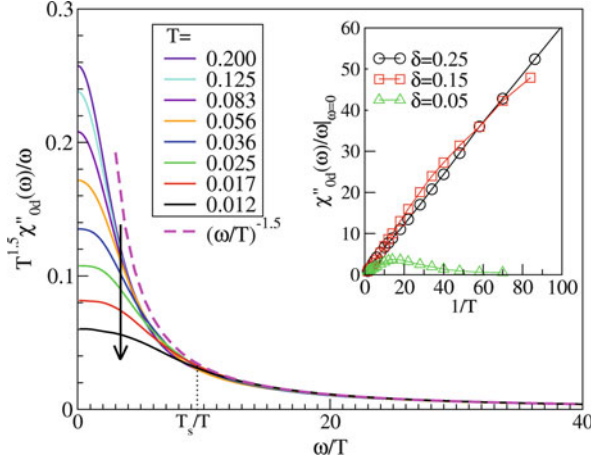
Fig. 9.21 (Taken from [40]) Plots of $T^{1.5} \chi''_{0d}(\omega)/\omega$ versus ω/T at the QC doping ($\delta = 0.15$) for $N_c = 16$. The *arrow* denotes the direction of decreasing temperature. The *curves* coincide for $\omega/T > 9 \approx (4t/J)$ defining a scaling function $H(\omega/T)$, corresponding to a contribution to $\chi'_{0d}(T) = \frac{1}{\pi} \int d\omega \chi''_{0d}(w)/w \propto 1/\sqrt{T}$ as found in Fig. 9.20. For $\omega/T > 9 \approx (4t/J)$, $H(\omega/T) \approx (\omega/T)^{-1.5}$ (*dashed line*). On the x-axis, we add the label $T_s/T \approx (4t/J)$, where T_s represents the energy scale where curves start deviating from H. The inset shows the unscaled zero-frequency result $\chi''_{0d}(\omega)/\omega|_{\omega=0}$ plotted versus inverse temperature

Unlike the pairing strength V_d, the d-wave pairing susceptibility χ_{0d} exhibits significantly different behaviors in the different doping regions around the QCP (Fig. 9.20). In the underdoped region ($\delta = 0.05$), also known as the pseudogap or NFL region, $\chi'_{0d}(\omega = 0)$ saturates to a finite value at low temperatures. At the critical doping, however, it diverges quickly when the temperature decreases, roughly following a $1/\sqrt{T}$ power-law behavior. The overdoped or FL region shows the expected log divergence.

To further understand the temperature-dependence of the d-wave pairing susceptibility at the quantum critical filling, we investigate $T^{1.5} \chi''_{0d}(\omega)/\omega$ and plot it in Fig. 9.21 as a function of ω/T. Scaled to this form, the curves from different temperatures collapse on each other so that

$$\frac{T^{1.5} \chi''_{0d}(\omega)}{\omega} = H\left(\frac{\omega}{T}\right) \approx \left(\frac{\omega}{T}\right)^{-1.5} \tag{9.46}$$

for $\omega/T \gtrsim 9 \approx 4t/J$, $J \approx 0.44t$. For $0 < \omega/T < 4t/J$, the BCS behavior appears and the curves deviate from $H(x)$ with $\chi''_{0d}(\omega)/\omega|_{\omega=0}$ weakly sublinear in $1/T$ as shown in the inset. Away from critical doping, the curves do not show such a collapse (not shown). $\chi''_{0d}(\omega)/\omega$ goes to zero with decreasing temperature (inset) in the underdoped region ($\delta = 0.05$) while it develops a narrow peak at low ω of width $\omega \approx T_X$ and height $\propto 1/T$ in the FL region (inset).
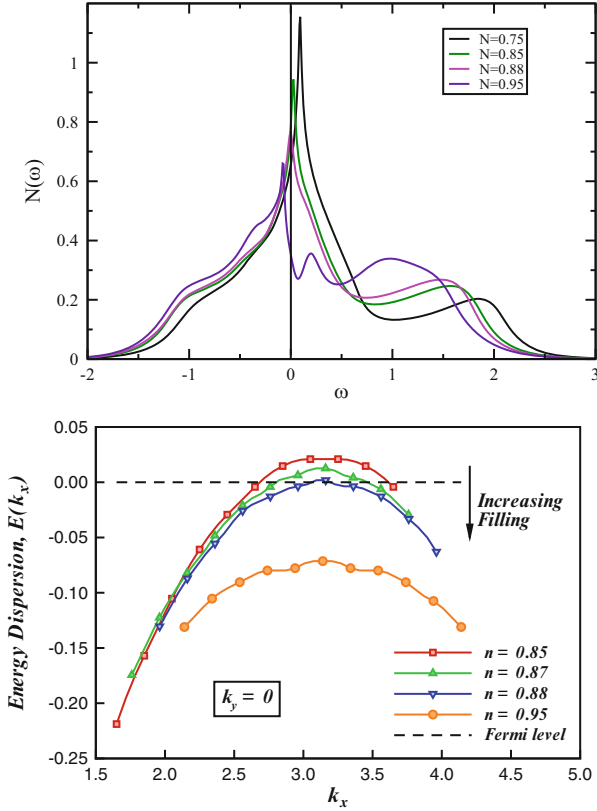
Fig. 9.22 (*Top*) Dependence of the density of states $N(\omega)$ with frequency ω for various fillings, where $U = 6t$, $4t = 1$, $N_c = 16$, and $T = 1/58$. The peak in $N(\omega)$ moves through $\omega = 0$ at the quantum critical filling and exhibits particle hole symmetry for small energies. (*Bottom*) Single-particle dispersion around the Fermi vector $\mathbf{k}_F$ along the antinodal direction $(\pi, 0)$. As the filling is increased, the saddle point in the dispersion moves through the Fermi level at the quantum critical filling, consistent with the density of states picture

Our results for χ_{0d} and V_d provide some understanding of the previously found [48] superconducting dome. As the doping increases, the pairing vertex V_d falls monotonically whereas $\chi'_{0d}(T)$ is strongly suppressed in the low doping or pseudogap region and enhanced at the critical and higher doping. These facts alone could lead to a dome-shaped region of superconductivity. Additionally, the algebraic divergence of the pairing susceptibility $\chi'_{0d}(T)$, as seen in Fig. 9.20, causes superconductivity to be strongly enhanced near the QCP so that one might expect $T_c \propto (V_d B)^2$, with $B = \frac{1}{\pi} \int \mathrm{d}x H(x)$, to replace the conventional BCS form in the FL region. This evidence supports the QCBCS scenario proposed by She and Zaanen [51].

Another interesting feature of the QCP is the proximity to the Fermi level of a van Hove singularity (vHS) in the single-particle dispersion. Many authors have

suggested that a vHS in the single-particle DOS at the Fermi level will enhance the superconducting transition temperature [60–63]. In an early DMFA study of the Hubbard model by Majumdar and Krishnamurthy [64], it was found that if the bare dispersion is modified such that the vHS is at the Fermi level for the noninteracting case, it remains pinned to the Fermi level for the interacting case. The noninteracting model studied here with $t' = 0$ has a vHS at the Fermi energy at half filling. The *new finding*, using the DCA method, is that the interactions produce a self-energy with sufficient momentum dependence so that the renormalized dispersion yields a vHS at the Fermi level at a finite filling. The interacting model has a gap at half-filling and as the filling is increased through the QCP, a vHS crosses the Fermi level near the QCP filling. This can be seen both in the DOS (top) and flat region in the energy dispersion (bottom) of Fig. 9.22. Unfortunately, the momentum dependence of the self-energy alone is not sufficient to reproduce the scaling of $\chi''_{0d}(\omega)$ found in Fig. 9.21. This scaling points towards a deeper origin of the enhanced divergence of the bare pairing polarization, such as that suggested by She and Zaanen in their quantum critical BCS scenario[51].

9.5 Conclusion

We have presented a pedagogical introduction to the DCA. We have described how coarse-graining methods can be used to derive both the DMFA and the DCA, which map the lattice to a self-consistently embedded cluster problem. We also showed how DMFA and DCA can be derived from a Φ functional. The DMFA is a local approximation while the DCA incorporates systematic nonlocal corrections. We have showed how the DCA is used to study the Hubbard model and the evidence it provides for the presence of a QCP underneath the superconducting dome. This QCP is the terminus of a line of second order phase separation transitions. Finally we have seen that the QCP may explain the relatively high superconducting critical temperature through an enhancement of the pairing susceptibility at the critical doping. In brief, the DCA provides an efficient tool to study correlated electron systems.

References

1. J. Hubbard, Proc. R. Soc. A**2**76, 238(1963)
2. M.C. Gutzwiller, Phys. Rev. Lett. **10**, 159(1963)

3. J. Kanamori, Prog. Theor. Phys. **30**, 257(1963)
4. Proceedings of the International Conference on Itinerant-Electron Magnetism. Physica B+C **9**1 (1977); for a review about the theory of the Hubbard model see also D. Vollhardt, Rev. Mod. Phys. **56**, 99(1984)
5. E.H. Lieb, F.Y. Wu, Phys. Rev. Lett. **20**, 1445 (1968)
6. H. Frahm, V.E. Korepin, Phys. Rev. B **42**, 10533 (1990)
7. N. Kawakami, S.-K. Yang, Phys. Rev. Lett. **65**, 2309 (1990)
8. G. Czycholl, J. Mag. Mag. Mat. **47,48**, 350 (1985)
9. W. Metzner, D. Vollhardt, Phys. Rev. Lett. **62**, 324 (1989)
10. P.G.J. van Dongen, D. Vollhardt, Phys. Rev. Lett. **65**, 1663 (1990)
11. Y. Kuramoto, Theory of Heavy Fermions and Valence Fluctuations: Proceedings of the Eighth Taniguchi Symposium, Shima Kanko, Japan, April 10–13, 1985 Eds T. Kasuya, T. Saso (Springer Series in Solid-State Sciences Vol 62) 152–162
12. C. Kim, Y. Kuramoto and T. Kasuya, J. Phys. Soc. Japan **5**9, 2414 (1990)
13. E. Müller-Hartmann, Z. Phys. B **74**, 507 (1989)
14. M.H. Hettler, A.N. Tahvildar-Zadeh, M. Jarrell, T. Pruschke, H.R. Krishnamurthy, Phys. Rev. B **58**, 7475 (1998)
15. M.H. Hettler, M. Mukherjee, M. Jarrell, H.R. Krishnamurthy, Phys. Rev. B **61**, 12739 (2000)
16. M. Jarrell Phys. Rev. Lett. **69**, 168 (1992)
17. T. Pruschke, M. Jarrell, J.K. Freericks, Adv. in Phys. **42**, 187 (1995)
18. A. Georges, G. Kotliar, W. Krauth, M.J. Rozenberg, Rev. Mod. Phys. **68**, 13 (1996)
19. R.M. Fye, J.E. Hirsch, Phys. Rev. B **38**, 433 (1988)
20. M. Jarrell, Th. Maier, C. Huscroft, S. Moukouri, Phys. Rev. B **64**, 195130/1–23 (2001)
21. M. Jarrell, J.E. Gubernatis, Phys. Rep. **269**, 3 (1996)
22. V. Zlatić, B. Horvatić, Sol. St. Comm. **75**, 263 (1990)
23. G. Baym, L.P. Kadanoff, Phys. Rev. **124**, 287, (1961)
24. C. Huscroft, M. Jarrell, Th. Maier, S. Moukouri, A.N. Tahvildarzadeh, Phys. Rev. Lett., **86**, 3691 (2001)
25. Th. Maier, M. Jarrell, Th. Pruschke, J. Keller, Eur. Phys. J. B **13**, 613 (2000)
26. N.E. Bickers, D.J. Scalapino, S.R. White, Phys. Rev. Lett. **62**, 961 (1989)
27. P.G.J. van Dongen, Phys. Rev. B **50**, 14016 (1994)
28. A. Schiller, K. Ingersent, Phys. Rev. Lett. **75**, 113 (1995)
29. A.A. Abrikosov, L.P. Gorkov, I.E. Dzyalishinski, *Methods of Quantum Field Theory in Statistical Physics* (Dover, New York, 1975)
30. S. Chakravarty, R.B. Laughlin, D.K. Morr, C. Nayak, Phys. Rev. B **63**, 094503 (2001)
31. S. Kivelson, E. Fradkin, V. Emery, Nature (London) **393**, 550 (1998)
32. M. Vojta, Y. Zhang, S. Sachdev, Phys. Rev. B **62**, 6721 (2000)
33. S. Sachdev, Rev. Mod. Phys. **75**, 913 (2003)
34. S. Sachdev, Nat. Phys. **4**, 173 (2008)
35. C.M. Varma, Phys. Rev. Lett. **83**, 3538 (1999)
36. S. Chakraborty, D. Galanakis, P. Phillips, Phys. Rev. B **82**, 214503 (2010)
37. N.S. Vidhyadhiraja, A. Macridin, C. Sen, M. Jarrell, M. Ma, Phys. Rev. Lett. **1**02, 206407 (2009)
38. A. Macridin, M. Jarrell, T. Maier, D.J. Scalapino, Phys. Rev. Lett., **99**, 237001 (2007)
39. Th. A. Maier, Th. Pruschke, M. Jarrell, Phys. Rev. B **66**, 075102 (2002)
40. S.-X. Yang, H. Fotso, S.-Q. Su, D. Galanakis, E. Khatami, J.-H. She, J. Moreno, J. Zaanen, M. Jarrell, Phys. Rev. Lett ̇ **1**06, 047004 (2011)
41. K. Mikelsons, E. Khatami, D. Galanakis, A. Macridin, J. Moreno, M. Jarrell, Phys. Rev. B **80**, 140505(R) (2009)
42. A.L. Fetter, J.D. Walecka, *Quantum Theory of Many-Particle Systems* (McGraw-Hill, New York, 1971)
43. M. Crisan, C.P. Moca, J. Supercond. **9**, 49 (1996)
44. F. Werner, O. Parcollet, A. Georges, S.R. Hassan, Phys. Rev. Lett. **95**, 056401 (2005)
45. Th. Maier, M. Jarrell, Th. Pruschke, M.H. Hettler, Rev. Mod. Phys. **77**, 1027 (2005)

46. C. Huscroft, R. Gass, M. Jarrell, Phys. Rev. B **6**1, 9300 (2000)
47. A.K. McMahan, C. Huscroft, R.T. Scalettar, E.L. Pollock, J. Comp. Aided Mater. Des. **5**, 131 (1998)
48. E. Khatami, K. Mikelsons, D. Galanakis, A. Macridin, J. Moreno, R.T. Scalettar, M. Jarrell, Phys. Rev. B **81**, 201101(R) (2010)
49. A. Macridin, M. Jarrell, Th. Maier, Phys. Rev. B **74**, 085104 (2006)
50. K. Haule, G. Kotliar, Phys. Rev. B **76**, 092503 (2007)
51. J.-H. She, J. Zaanen, Phys. Rev. B **8**0, 184518 (2009)
52. C. Castellani et al., Z. Phy. B **103**, 137–144 (1997)
53. E.-G. Moon, A. Chubukov, J. Low Temp. Phys. **1**61, 263 (2010)
54. N. Bulut et al., Phys. Rev. B **47**, 6157(R) (1993)
55. M. Jarrell et al., EuroPhys. Lett. **56**, 563 (2001)
56. T.A. Maier et al., Phys. Rev. Lett. **95**, 237001 (2005)
57. T.A. Maier et al., Phys. Rev. Lett. **96**, 047005 (2006)
58. S.-X. Yang, H. Fotso, J. Liu, T.A. Maier, K. Tomko, E.F. DAzevedo, R.T. Scalettar, T. Pruschke, M. Jarrell, Phys. Rev. E **80**, 046706 (2009)
59. T.A. Maier et al., Phys. Rev. B **76**, 144516 (2007)
60. J. Labbè, J. Bok, Europhys. Lett. **3**, 22 (1987)
61. J. Friedel, J. Phys. (Paris) **48**, 10 (1987)
62. D.M. Newns, H.R. Krishnamurthy, P.C. Pattnaik, C.C. Tsuei, C.L. Kane, Phys. Rev. Lett. **69**, 8 (1992)
63. R.S. Markiewicz, Phys. Chem. Solids **58**, 8 1179–1310 (1997)
64. P. Majumdar, H.R. Krishnamurthy, cond-mat/9604057v1 (1996)